Analytical Study of Solution-Processed Tin Oxide as Electron Transport Layer in Printed Perovskite Solar Cells

Valentina Rohnacher, Florian Ullrich, Helge Eggers, Fabian Schackmar, Sebastian Hell, Adriana Salazar, Christian Huck, Gerardo Hernandez-Sosa, Ulrich W. Paetzold, Wolfram Jaegermann, and Annemarie Pucci*

Solution-processed tin oxide (SnO_x) electron transport layers demonstrate excellent performance in various optoelectronic devices and offer the ease of facile and low cost deposition by various printing techniques. The most common precursor solution for the preparation of SnO_x thin films is $SnCl_2$ dissolved in ethanol. In order to elucidate the mechanism of the precursor conversion at different annealing temperatures and the optoelectronic performance of the SnO_x electron transport layer, phonon and vibrational infrared and photoelectron spectroscopies as well as atomic force microscopy are used to probe the chemical, physical, and morphological properties of the SnO_x thin films. The influence of two different solvents on the layer morphology of SnO_x thin films is investigated. In both cases, an increasing annealing temperature not only improves the structural and chemical properties of solution-processed SnO_x, but also reduces the concentration of tin hydroxide species in the bulk and on the surface of these thin films. As a prototypical example for the high potential of printed SnO_x layers for solar cells, high performance perovskite solar cells with a stabilized power conversion efficiency of over 15% are presented.

V. Rohnacher, S. Hell, Dr. C. Huck, Prof. A. Pucci
Kirchhoff Institute for Physics
Heidelberg University
Im Neuenheimer Feld 227, Heidelberg 69120, Germany
E-mail: pucci@kip.uni-heidelberg.de
V. Rohnacher, Dr. F. Ullrich, H. Eggers, F. Schackmar,
S. Hell, A. Salazar, Dr. G. Hernandez-Sosa, Dr. U. W. Paetzold,
Prof. W. Jaegermann, Prof. A. Pucci
InnovationLab
Speyerer Straße 4, Heidelberg 69115, Germany
Dr. F. Ullrich, A. Salazar, Prof. W. Jaegermann
Material Science Department
Surface Science Division
Technische Universität Darmstadt
Petersenstraße 32, Darmstadt 64287, Germany
H. Eggers, F. Schackmar, Dr. G. Hernandez-Sosa, Dr. U. W. Paetzold
Light Technology Institute
Karlsruhe Institute of Technology
Engesserstraße 13, Karlsruhe 76131, Germany

1. Introduction

The rapid increase in the power conversion efficiency (PCE) of perovskite solar cells (PSCs) from 3.8% to 25.2%[1–3] within less than a decade can be attributed to a considerable extent to the impact of proper electron transport layers (ETLs).[4] Due to the high transparency in the visible region,[4,5] the large bandgap,[6] the low valence and conduction band,[4,7] and the high charge carrier mobility[8] tin oxide is an excellent material for usage in ETLs.[5,9,10] For this reason, it is widely used in a variety of technological applications like optoelectronic devices[6,9] or sensors.[11,12] Compared to other metal oxides such as TiO_x or ZnO, SnO_x offers divers advantages including better optical and chemical stability.[4,9] Moreover, due to the favorable interface properties of SnO_x/perovskite heterojunctions,[4,13] SnO_x has great potential as highly efficient ETL in perovskite solar cells (PSCs).

Furthermore, SnO_x can be processed from solution, which allows for deposition by printing techniques and brings advantages like low production costs, usability of flexible substrates and easy-to-scale, additive manufacturing processes into tangible reach.[6,14,15]

A promising printing technology for the fabrication of solar cells is inkjet printing, which is a fast, scalable, and highly material-efficient deposition method.[16] For inkjet printing of SnO_x films, two possible routes exist. On the one hand, it can be processed from precursor solutions, and on the other hand from nanoparticle-based dispersions. As the former is less prone to agglomeration and therefore promises advantages for inkjet printing, this work focuses on the analysis of a popular SnO_x precursor material, namely $SnCl_2 \cdot 2H_2O$.

Although substantial improvements have been demonstrated with solution-processed SnO_x as ETL, there are still a number of challenges on the way to mass production, including improved lifetimes, further increase of PCE and better reproducibility SnO_x-based solar cell.[4,17]

In order to achieve these goals and render possible improvements comprehensible, a better understanding of the properties of solution-processed SnO_x is necessary. In addition to the precursor concentration,[6] the choice of the solvent and the

**ADVANCED
SCIENCE NEWS**
www.advancedsciencenews.com

**ADVANCED
MATERIALS
TECHNOLOGIES**
www.advmattechnol.de

annealing temperature are considered to be important factors affecting the morphology and the optoelectronic properties of SnO_x.[4] Although there are some hints,[4,18] a systematic and comprehensive study of these influences is missing. This is the gap we want to fill with the current work. In this respect, we systematically study the structural, chemical, and optoelectronic properties of SnO_x, and the influence on the PSCs device performance. Thus, the aim of this study is the characterization of solution-processed SnO_x thin films layers to achieve a better understanding of SnO_x as ETLs in order to improve the performance off SnO_x-based PSCs.

2. Results and Discussion

The solution-processed tin oxide thin films ($sSnO_x$) studied in this work were spin-casted from a 0.2 M tin-II-chloride dehydrate ($SnCl_2 \cdot 2H_2O$)[10] precursor solution on silicon and ITO substrates using different solvents (for more details see Experimental section). After spin-casting, the films were annealed in ambient atmosphere at temperatures ranging between 130 °C and 400 °C. In order to develop a better understanding of the conversion process and the fundamental properties of the solutions-processed tin oxide layers, we applied infrared (IR) spectroscopy, scanning probe microscopy, photoelectron spectroscopy (XPS), and UV–vis ellipsometry for the characterization of differently prepared tin oxide thin films. The results will be discussed in the following.

2.1. Atomic Force Microscopy Images

Atomic force microscopic (AFM) images of $sSnO_x$ thin films annealed at different temperatures illustrate the morphological development of the thin films upon precursor conversion, see **Figure 1**. The samples were prepared according to the protocol described in detail in Experimental section. The $sSnO_x$ thin films of Figure 1a–d and e–h are prepared from a precursor solution using methoxyethanol and ethanol as solvents, respectively. It is evident that the choice of the solvent significantly alters morphology. While for methoxyethanol as solvent the layer is rather smooth, the layer prepared from ethanol-based solution exhibits a significantly enhanced roughness and inhomogeneous, circular structures up to 30 nm height and 500 nm width. Given that the two solvents differ in their respective boiling points (T(ethanol) = 78 °C, T(methoxyethanol) = 124 °C), the morphological differences are most apparent for the precursor layer; it is thus indicated that the different morphology is arising during the spin-coating process and not during the subsequent annealing process. However, even elevated annealing temperatures up to 400 °C do not fully omit the morphological differences of the layers processed from the two types of solution systems. Moreover, the thin films prepared from an ethanol solution exhibit a substructure with grains similar to that of the methoxyethanol-based samples at lower annealing temperatures is seen in the AFM image (Figure 1h).

The $sSnO_x$ layers based on methoxyethanol form rather homogeneous nanoparticle layers. Methoxyethanol has a higher boiling point compared to water and ethanol, which provides the precursor more time to form a homogeneous layer before the solvent evaporates.[19,20] The morphologies of the tin oxide layers hardly differ for annealing temperatures between 130 °C and 200 °C and are ascribed to a granular surface morphology that exhibits a very low roughness. The crystallinity of the tin oxide layers increases with increasing annealing temperature.[21–23] The tin oxide layer annealed at 250 °C shows small grains (see Figure 1c). The well-defined grains and the higher roughness compared to morphologies for lower annealing temperatures indicate the increase in crystallinity and grain size which becomes particularly clear for $sSnO_x$ thin films annealed 400 °C (see Figure 1d).

2.2. Infrared Spectroscopy

The transmittance measurements shown in **Figure 2** are taken in the far infrared (FIR) (100–650 cm^{-1}) and mid infrared (MIR) (650–4000 cm^{-1}) spectral range. FIR measurements taken under various polarization conditions probe the optical phonons in the reststrahlen band of the material. This optical
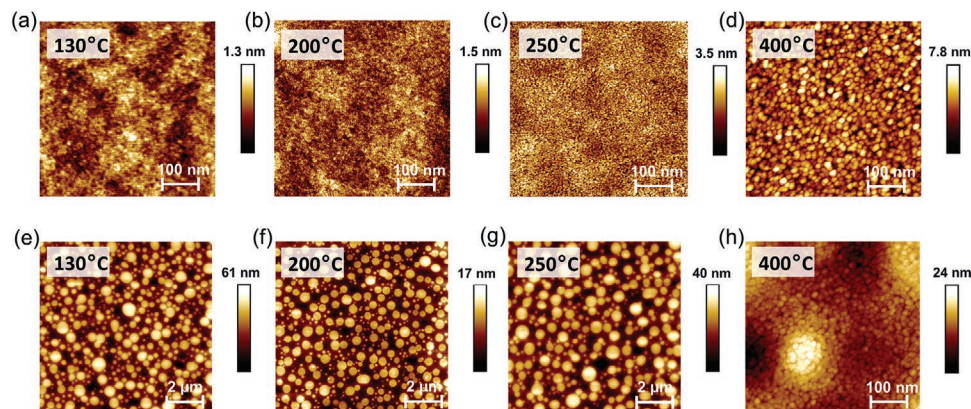

Figure 1. Surface morphology of solution-processed SnO_x thin films measured by AFM. The samples are prepared from different solvents systems: a–d) methoxyethanol and e–h) ethanol. The thin films are annealed at different temperatures 130 °C, 200 °C, 250 °C, and 400 °C. The AFM measurements are taken with the peak force tapping mode under ambient conditions. The scan area is 500 nm × 500 nm for (a–d) and (h). For a better overview, the scan area for (e–g) is 10 μm × 10 μm.
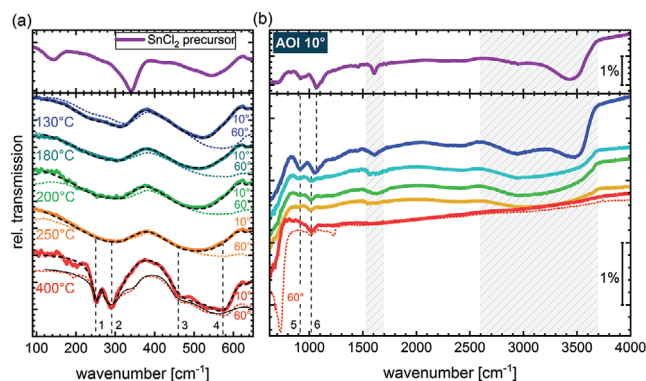
**ADVANCED
SCIENCE NEWS**

www.advancedsciencenews.com

**ADVANCED
MATERIALS
TECHNOLOGIES**

www.advmattechnol.de

Figure 2. a) FIR relative transmission spectra of solution-processed SnO_x thin films prepared from methoxyethanol-precursor solutions and annealed at 130 °C (blue), 180 °C (turquoise), 200 °C (green), 250 °C (orange), and 400 °C (red) measured under 10° (solid lines) and 60° (dashed lines) angle of incidence (AOI). The purple graph shows the spectra of a $SnCl_2$ precursor thin film before annealing. The modes 1–4, marked with the dashed vertical lines, indicate the TO modes of SnO_2 of the thin films annealed at 400 °C. The black dashed curves show the fit of the dielectric function of SnO_x with Gervais oscillators (see Supporting Information for details). b) The MIR spectra of SnO_x thin films show characteristic bands of $Sn(OH)_2$ at 1600 cm^{-1} and between 2700 and 3600 cm^{-1}, also strongly visible in $SnCl_2$ precursor thin film (purple graph). With increasing annealing temperature the precursor conversion is indicated by the decreasing $Sn(OH)_2$ mode and the decreasing mode 5 assigned to the precursor material. At 60° AOI (dashed spectrum) the Berreman mode[24] of crystalline SnO_2 is visible at 730 cm^{-1} for the thin film annealed at 400 °C.

phonon response strongly depends on the exact stoichiometry and the crystallinity (i.e., grain sizes and the grain packing) of the $sSnO_x$ thin films. The MIR region provides insight into molecular vibrations and, thus, conclusions about the chemical composition of possible species between tin oxide grains. Figure 2 shows $sSnO_x$ thin film spectra for the samples prepared with the methoxyethanol-based solution (see Figure S4, Supporting Information for ethanol as solvent).

Figure 2a shows the FIR spectra of five $sSnO_x$ samples (prepared with methoxyethanol-precursor solution) annealed at the different temperatures, each measured under two angles of incidence (AOI): 10° (which is referred to as normal incidence) and 60° (with an electric field component of the incoming IR light perpendicular to the layer).

For normal incidence, the pristine precursor layer (Figure 2a, purple spectrum) shows characteristic vibrational bands at 144 and 340 cm^{-1}, which can be assigned to tin chloride.[25] The band at 540 cm^{-1} is assigned to tin hydroxide, which is also apparent in the subsequent annealed layers until 250 °C.[26] The sample annealed at 130 °C still contains an amount of tin chloride, as shown in the shoulder of absorption mode at 321 cm^{-1}. The broad absorption band around 300 cm^{-1} can be attributed to vibrations of SnO.[27] The broad feature at about 500 cm^{-1} also fits into the range of SnO optical phonons.[26–28] These modes still appear in the transmission spectra for annealing temperatures of 130 °C to 250 °C.

The FIR spectra of the tin oxide layer annealed at 400 °C are clearly distinguishable from the samples annealed at lower temperatures. A Gervais oscillator model of the dielectric function of SnO_2, as described in the Supporting Information,

yields transversal optical (TO) resonance frequencies of 251, 290, 463, and 583 cm^{-1} (marked in in Figure 2a), which is in very good agreement with literature values for the TO mode of SnO_2[29–31] as shown in Table S1 (Supporting Information). With p-polarized IR radiation at an AOI of 60° TO phonons and also surface phonon polaritons (known as Berreman effect[24]) are excited. Assuming a perfect optically isotrope SnO_2 thin film, this polariton has the frequency of the longitudinal optical (LO) phonon.[24] The mode shifts to lower frequencies with film roughness and consequently is a measure of the film quality. Thus, in the transmission spectra for oblique incidence of light (Figure 2a, dashed graphs) of layers annealed at 130 °C to 250 °C, the TO and surface modes are superimposed, such that the absorption bands appear widened toward larger wave numbers. At 400 °C, an additional absorption band at 345 cm^{-1} appears, which corresponds to the surface mode of SnO_2.[29] Also in the adjacent MIR spectrum for 400 °C at 60° AOI (Figure 2b, red dashed graph) a surface mode at 730 cm^{-1} is visible, the occurrence of which suggests the formation of crystalline SnO_2 regions and which can be explained by the granular morphology of the thin film in Figure 1d. Thus, we conclude that the modes in the FIR indicate the presence of stoichiometric SnO_2 after annealing the thin films at 400 °C.

In the MIR region in Figure 2b, mode 5 at 920 cm^{-1} is assigned to $SnCl_2$. As expected, with increasing annealing temperature, this band decreases due to the conversion of $SnCl_2$ in SnO_2. The $SnCl_2$ band disappears around 250 °C. This means that chlorine is in the thin films up to at least 250 °C annealing temperature. Mode 6 just above 1000 cm^{-1} is assigned to SiO_x, a silicon oxide with unclear stoichiometry.[32,33] We hypothesized that the acidic $SnCl_2$ solution (pH < 1) oxidizes the silicon substrate, inducing additional oxide and, thereby, additional absorption bands.[33] At 1607 cm^{-1} an O—H deformation oscillation of stored water is apparent.[34] It decreases with increasing annealing temperature, indicating a decrease of water content. In the range between 2600 and 3700 cm^{-1} very broad absorption bands are visible which are caused by O—H stretching vibrations.[25] However, given that these bands do not decrease with increasing annealing temperature to the same extend as the O—H bending band of water at 1607 cm^{-1}, they are not assigned to water but to tin hydroxide. The red spectra from a $sSnO_x$ film annealed at 400 °C shows no O—H absorption modes anymore, indicating a fully converted tin oxide layer with no precursor remains. The MIR results for ethanol as solvents are only marginally different to those for methoxyethanol, suggesting both solvents only lead to different morphologies but not to different chemical species after annealing.

2.3. Photoelectron Spectroscopy

Next, we discuss XPS measurements that allow determining the surface composition of $sSnO_x$ electron transport layers. In contrast to IR, XPS is a highly surface sensitive technique and thus yields complementary results. Still, due to the small thickness of the films in the present case, there is a significant overlap of the results of both methods. **Figure 3**a–c shows XPS spectra of $sSnO_x$ films annealed at different temperatures. Two
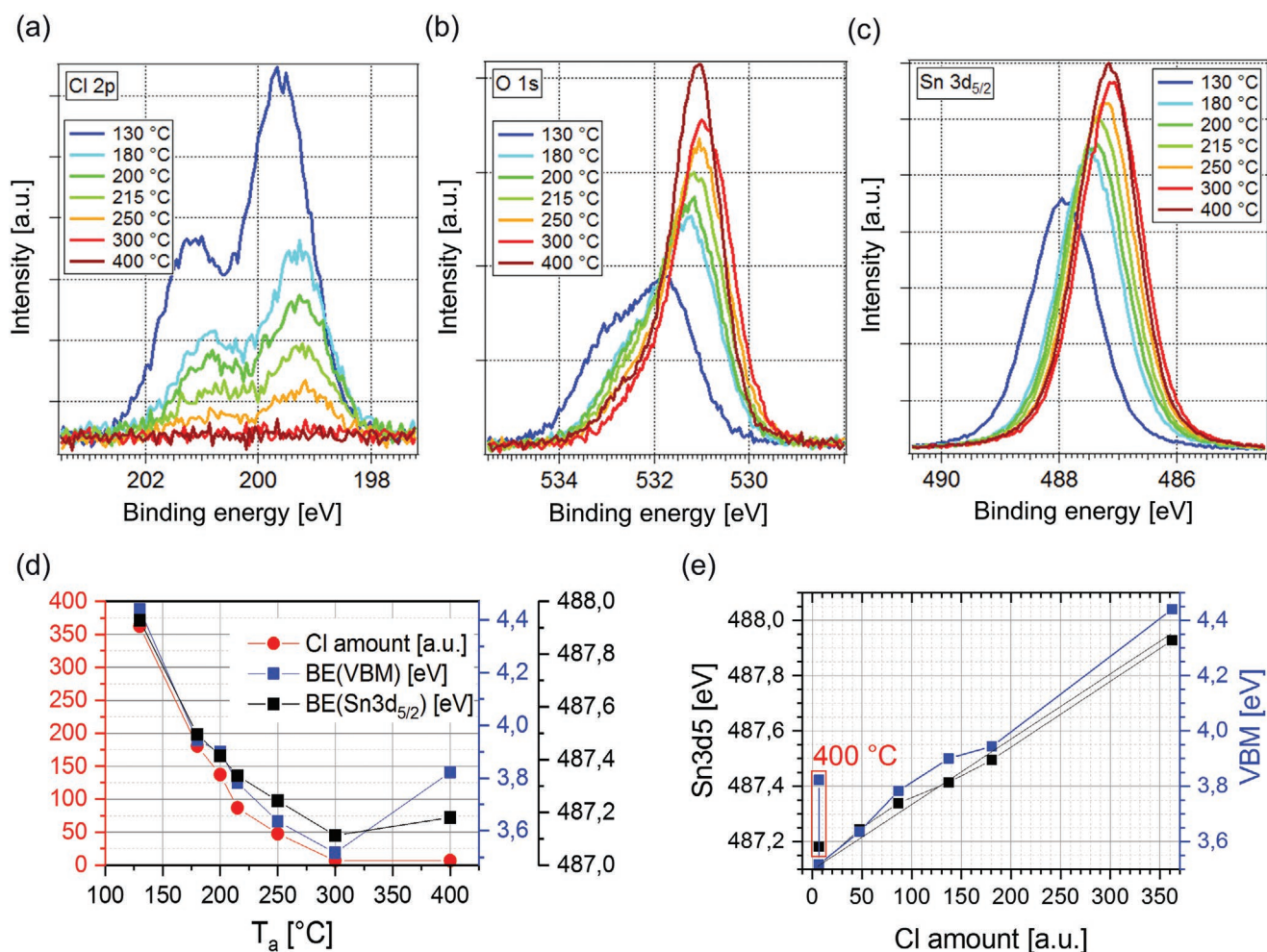
Figure 3. XPS detail spectra of the a) Cl 2p region, b) O 1s region, and c) Sn $3d_{5/2}$ region of solution-processed SnO_x for samples annealed at different temperatures. Less chlorine and less hydroxide obviously influence the Fermi level position. d) A quantitative analysis of the spectra in (a–c). The chlorine amount (red) is defined as integral intensity of the Cl 2p signal and correlates to the atomic concentration of chlorine. The binding energy (BE) positions of both the Sn $3d_{5/2}$ peak (black) and the valance band maximum (VBM) (blue, spectra not shown) are displayed. e) Both the Sn $3d_{5/2}$ peak position (black) and the VBM (blue) are plotted against the chlorine amount. An approximately linear relationship is obtained for annealing temperature below 300 °C and the direction of the Fermi level shifts changes when increasing the annealing temperature from 300 °C to 400 °C.

major changes in the chemical composition are observed, when higher annealing temperatures are chosen.

First, the atomic concentration of chlorine, which is a residue of the precursor as discussed above, is constantly decreasing (Figure 3a). For $sSnO_x$ thin films annealed at 300 °C or higher, the atomic concentration of chlorine has dropped below the detection limit of XPS and the film can be seen as free of chlorine. These observations are in very good agreement with the IR results.

Second, the high-binding energy shoulder in the O 1s spectrum shown in Figure 3b is reduced, indicating a decrease of hydroxidic (OH) species with increased annealing temperature. This agrees to the IR results described above and we can ascribe this high-binding energy component to $Sn(OH)_2$. However, while IR spectroscopy cannot detect any signal from tin hydroxide in films annealed at 400 °C, a small shoulder at high-binding energies still exists in the O 1s spectrum. Due to the strong phonon modes observed with IR, we believe that the

main contribution to this component in the O 1s spectrum is rather due to OH groups at the surface than in the bulk. The small size of the high-binding energy component indicates a coverage in the submonolayer range,[35] which is detectable with XPS but not with IR spectroscopy. We conclude a film, which is largely free of OH in the bulk but has OH groups at the surface with a coverage in the submonolayer range. A similar result has previously been obtained for NiO films.[33,35] It was found that OH has formed on the surface during the air-exposure of the annealed film in the time between the annealing process and the analysis in UHV, while the bulk of the films where largely free of OH.

The described changes of the chemical composition are reflected in a change of the Fermi level position. This is shown by the shifts in binding energy of the spectra in Figure 3a–c. Less chlorine and less hydroxide obviously shift the Fermi level closer to the valence band maximum (VBM). This qualitative observation was quantified and is displayed in Figure 3d,

where the binding energy positions of both VBM (blue) and the Sn $2p_{5/2}$ peak (black) as well as the chlorine amount (red, defined as integral intensity of the Cl 2p signal) are plotted against the annealing temperature (T_a). To further investigate the correlation between chlorine amount and the Fermi level position in the films, both the Sn $3d_{5/2}$ peak position (black) and the VBM (blue) are plotted against the chlorine amount in Figure 3e. An approximately linear relationship is obtained. This is reminiscent of a doping mechanism, in which the amount of dopant (here, chlorine) determines the Fermi level position in the film. For further discussion of the doping mechanism (Supporting Information).

Interestingly, the inverse trend is apparent for the highest annealing temperatures (>400 °C). Here, the Fermi level shifts back toward the conduction band, away from the valence band (see red rectangle in Figure 3e). Furthermore, the energetic distance between the VBM and the Sn $3d_{5/2}$ peak position changes, whereas this distance has remained unchanged for annealing temperatures below 300 °C. This suggests a structural change in the film and is explainable by the transition to crystalline SnO_2 as observed with IR spectroscopy.

We conclude that below 300 °C annealing temperature the position of the Fermi level is dominated by the amount of chlorine in the film, while of course as well an influence of the hydroxide amount has to be considered. In contrast, the Fermi level shift reverses its direction when the annealing temperature is increased to above 300 °C. While the first regime is dominated by changes of the chemical composition, the reason for the Fermi level shift above 300 °C appears to be related to the transition from disordered tin oxide to crystalline SnO_2. Since the choice of solvent can also have a decisive effect on the film properties, additional samples were prepared with methoxyethanol. Despite the morphological differences between the two samples, the XP spectra do not show any noticeable influence and even the work function is almost identical (Figure S6, Supporting Information).

2.4. Perovskite Solar Cells

Solution processed SnO_x thin films have been established as high performance electron transport layer (ETL) for efficient perovskite solar cells (PSCs) and have been successful processed from precursor solutions as well as nanoparticle-based dispersions on mostly laboratory scale.[18,36–38] The up-scaling of these efficient small-area devices is one of the main challenges of the perovskite photovoltaic technology. To meet this a number of printing and coating techniques are under investigation.[39] Here inkjet printing is among the more promising technologies due to its recent advances in the field of printed PSCs[16] and the overall success of this technology in mass production of for example organic light emitting diodes.[40–42] Inkjet printing is a fast, scalable and highly material-efficient deposition method and offers the possibility to print arbitrary design patterns without the need for masks. Depending on the intended feature size, print heads with different nozzle diameter are available. However, these print heads can be a major bottleneck for inkjet printing of nanoparticles: Above-average sized or agglomerated nanoparticles are prone to clog single printing nozzles, leading to rough structures or in worst case to pinholes in the layer resulting in leakage currents.[43] A precursor-based approach of SnO_x might have an advantage over the deposition of nanoparticle dispersions.

Here, we demonstrate the feasibility of PSCs with inkjet-printed (IJP) $sSnO_x$ layers. Therefore, a $sSnO_x$-ink based on the presented methoxyethanol and a modified ethanol precursor system is IJP on glass substrates with indium doped tin oxide (ITO) electrodes. An IJP triple cation perovskite (TCP) layer, a spin-coated 2,2′,7,7′-tetrakis[N,N-di(4-methoxyphenyl)amino]-9,9′-spirobifluorene (spiro-OMeTAD) and an evaporated gold electrode complete the device stack (**Figure 4**a). This architecture has been used successfully for fabrication of spin-coated PSCs.[18,36–38,44] The IJP $sSnO_x$ layer is annealed at maximum temperatures of 250 °C, since ITO starts to degrade at roughly 250–325 °C.[45] In a preliminary test batch with spin-coated $sSnO_x$, 180 °C annealed samples appear to result in better working ETLs, while the precursor solvent seems to have a minor influence on the device performance (Figure S7, Supporting Information).

PSCs with IJP $sSnO_x$ from as-prepared precursor solutions (here methoxyethanol is used) and IJP TCP show average PCEs of 8.3% (3.9%), derived from backward (forward) direction current–voltage characteristic. Compared to the average PCE of reference devices using spin-coated SnO_x nanoparticles as ETL of 13.1% (11.9%) this is significantly lower (compare Figure 4b). In particular, the devices with $sSnO_x$ show an increased hysteresis behavior, which is attributed to a significant drop of open-circuit voltage (V_{OC}) for devices with $sSnO_x$ in forward current–voltage scan direction (Figure 4c), indicating an insufficient charge carrier extraction at the ETL-absorber interface. Overall, the large spread in performance for both $sSnO_x$ and SnO_x nanoparticles (compare Figure S8, Supporting Information) suggests that the PSCs presented here are not fully optimized yet. To improve the printability and drying of the $sSnO_x$ wet-film the precursor solvent is varied to a mixture of ethanol and 1-butanol (3:1 vol). The PSCs fabricated with the modified $sSnO_x$ display an enhanced average PCE of 16.8% (10.5%) in backward (forward) current–voltage characteristic. The champion device displays a single scan efficiency of 18.8% and an average stabilized power conversion efficiency (SPCE) of 15.2% in maximum power point tracking over 5 min (Figure 4d). Although this device still exhibits a significant hysteresis, these high power conversion efficiencies and stable power output are remarkable results for PSCs with both IJP ETL and absorber. In a comparable approach with two IJP layers, Huckaba et al. so far achieved a champion device performance of 14.1% PCE and 12% SPCE for an IJP mesoporous TiO_x ETL and an IJP multication perovskite absorber, derived from a single-direction current–voltage characteristic.[46] The hysteresis behavior is comparable to an extended approach with three IJP layers, consisting of a tungsten oxide nanoparticle ETL and a single-cation perovskite absorber (and an IJP spiro-OMeTAD hole transport layer) with a PCE of 10.7% in backward and 6.4% in forward scan direction.[47] One way to reduce hysteresis behavior in combination with IJP perovskite absorbers has been reported for evaporated C_{60} interlayers on solution-processed compact-TiO_x reaching 17.6% PCE (16.6).[48] Providing further optimization concerning the device fabrication, $sSnO_x$ is a very promising

**ADVANCED
SCIENCE NEWS**
www.advancedsciencenews.com

**ADVANCED
MATERIALS
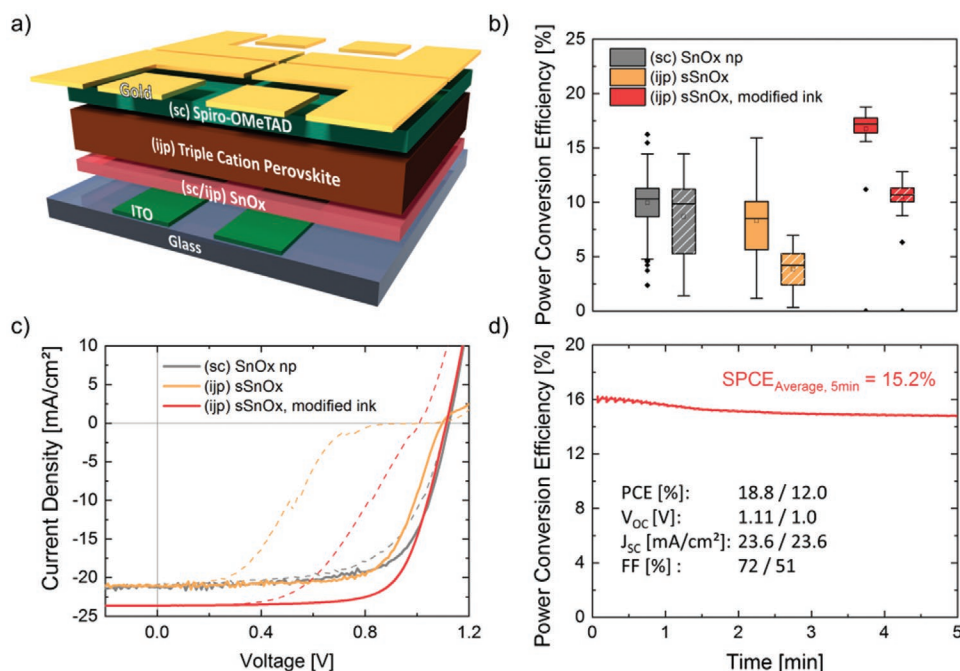TECHNOLOGIES**
www.advmattechnol.de

Figure 4. a) Schematic presentation of the fabricated perovskite solar cell (PSC) architecture glass/ITO/SnO$_x$/TCP/spiro-OMeTAD/gold. b) Overview over several batches of PSCs solution-processed sSnO$_x$ (IJP) and SnO$_x$ np (spin-coated) as reference. For every batch power conversion efficiencies (PCEs) derived from backwards (left box) and forward current-voltage scan (right box) are shown. For batch 1 to 3 identical parameters were used to deposit the sSnO$_x$ (180 °C, methoxyethanol), whereas for batch 4 the ink was optimized slightly for the printing process (180 °C, ethanol:butanol (3:1)). c) Current–voltage characteristics of champion device with IJP precursor-based tin oxide (from batch 4). d) Stabilized PCE (SPCE) of champion device.

ETL for solution-based upscaling processes, strengthening the importance of this analytic study.

3. Conclusion

In summary, this work investigates the importance of the correct annealing temperature of solution processed SnO$_x$ ETLs to the chemical and optoelectronic properties of sSnO$_x$ thin films. It is shown that the morphology of the sSnO$_x$ thin films is strongly altered by the choice of solvents. The sSnO$_x$ film from a precursor solution based on ethanol have an inhomogeneous surface morphology. In contrast, a precursor solution based on methoxyethanol leads to homogeneous thin films of densely packed small grains. The choice of the precursor solvent shows no relevant influence on the spectroscopic data from IR and XPS, and only minor influence on the device performance. Furthermore, we found that increasing annealing temperature leads to less tin hydroxide and less chlorine in the films. The combination of AFM, IR, and XPS results enabled us to unveil the transition from SnO$_x$ to stoichiometric SnO$_2$ by the change of the grain size, phonon modes, and Fermi level shift above 300 °C. In terms of prototype perovskite solar cells, the champion device reported in this work displays a very remarkable single scan efficiency of 18.8% and a stabilized power conversion efficiency of over 15% in maximum power point tracking over 5 min. Although there is still a significant hysteresis, this high and stable power output is a very remarkable result for PSCs with two inkjet-printed layers. Providing further optimization in the device fabrication, SnO$_x$ has strong potential

to serve as an ETL for solution-based upscaling processes, strengthening the importance of this analytic study. In conclusion, this work contributes to a better general understanding of chemical and electronic processes of solution-processed SnO$_x$ and thus supports the interpretation of SnO$_x$-based device characteristics and provides another building block on the way to the improvement of solar cells.

4. Experimental Section

Materials: Tin(II) chloride dihydrate (99.995% trace metal basis) and 2-methoxyethanol (anhydrous, 99.8%) were purchased from Sigma-Aldrich and anhydrous ethanol from VWR. Reagents were used without further purification.

sSnO$_x$ Thin Film Preparation: Tin oxide thin films of ≈25 nm thickness were fabricated by spin-coating tin chloride dihydrate solution on silicon substrates. The 13 × 13 mm² silicon substrates with native oxide were cleaned sequentially for each 15 min with acetone and 2-propanol in an ultrasonic bath, dried with nitrogen gas. The precursor material tin chloride dehydrate was dissolved in ethanol and methoxyethanol, respectively. The solution concentration was 0.2 M and stirred at 50 °C under ambient condition at least for 15 h prior to deposition by spin-coating on to the silicon substrates (2000 rpm for 30 s, acceleration: 1000 rpm s⁻¹). The films were then thermally annealed at different temperatures between 130 °C and 400 °C) for 60 min in ambient clean room atmosphere and immediately afterwards transferred to the respective measurement setups. The film thicknesses of the sSnO$_x$ layer was determined by UV–vis ellipsometry.

AFM: Atomic force microscopy (AFM) measurements were done with a Bruker NanoScope IV atomic force microscope in ScanAsyst mode under ambient conditions. The scanning frequency was set between 0.5 and 0.7 Hz.

IR: Infrared spectroscopy (IR) measurements were done using a Vertex 80v (Bruker) Fourier-transform (FT) IR spectrometer equipped with a nitrogen-cooled mercury cadmium telluride (MCT) detector for the mid-infrared range and a helium-cooled bolometer detector for the far-infrared range. The instrument was evacuated (3 mbar) and the sample compartment was flushed with a constant nitrogen flux during the measurements for MIR measurements. For FIR measurements both instrument and sample compartment were evacuated (3 mbar). The spectra were measured with p-polarized light and are an average about 200 scans with a resolution of 4 cm^{-1}. Each sSnO$_x$ measurement was divided by a reference spectrum of a clean silicon substrate, thus giving the relative transmission T of the sSnO$_x$ thin film. The measured angle-resolved transmission spectra of sSnO$_x$ in the far infrared range was modeled using the commercially available software package SCOUT.[49]

PES: Photoelectron spectroscopy measurements were performed using the VersaProbe II of PHI equipped with a monochromatized Al K$_\alpha$ X-ray ($h\nu = 1486$ eV) source and an Omicron HIS 13 helium discharge lamp (HeI: $h\nu = 21.22$ eV) as excitation sources for X-ray photoelectron spectroscopy XPS and UPS. Secondary electron edges were measured with XPS with a bias of 7 V and calibrated via the work function of in situ sputter-cleaned Ag foil determined by ultraviolet photoelectron spectroscopy (UPS). Here, the Ag UP spectrum was referenced to its Fermi level position. The base pressure of the measuring chamber during all experiments was kept in the 10^{-9} mbar regime. The take-off angle was 90°.

Perovskite Solar Cells Fabrication: The triple cation perovskite (TCP) was deposited as described in literature.[50] CH(NH$_2$)$_2$I (FAI, 0.6 M, GreatCell Solar), PbI$_2$ (0.66 M, Alfa Aesar, ultra-dry), CH$_3$NH$_3$Br (MABr, 0.12 M, GreatCell Solar) and PbBr$_2$ (0.12 M, TCI Chemicals) are dissolved in a mixture of *N,N*-dimethylformamide (DMF, Sigma-Aldrich), dimethyl sulfoxide (DMSO, Sigma-Aldrich), and gamma-butyrolactone (GBL, Sigma-Aldrich) in a ratio 28:26:46 (volume percentage). A 1.5 M CsI (Alfa Aesar) in DMSO was prepared as a second solution and then added to the first one to get a 0.75 M TCP solution with the targeted composition Cs$_{0.10}$FA$_{0.75}$MA$_{0.15}$Pb(Br$_{0.15}$I$_{0.85}$)$_3$. The ink was filtered through a 0.45 μm pore size polytetrafluoroethylene (PTFE) filter. The precursor SnO$_x$ solution for inkjet printing was prepared as the spin-coated pendant. Spiro-OMeTAD (Luminescence Technology) was dissolved in chlorobenzene (80 mg mL^{-1}) and doped with 28.5 μL 4-*tert*-butylpyridin (4tBP) and 17.5 μL lithium *bis*(trifluoromethanesulfonyl)imide (Li-TFSI) 520 mg mL^{-1} in acetonitrile.

A Meyer Burger PiXDRO LP50 with a print head module for 10 pl Fujifilm cartridges (Dimatix DMC-16 610) was used for printing the sSnO$_x$ and perovskite thin films in ambient conditions (≈21 °C, ≈45% relative humidity). Prepatterned glass/ITO substrates (Luminescence Technology) were cleaned consecutively in Hellmanex, DI water, acetone and isopropanol (IPA) in an ultrasonic bath for 5 min each, followed by an oxygen plasma-cleaning step for 5 min and again 5 min acetone and IPA in an ultrasonic bath. The IJP sSnO$_x$ was deposited (400 dpi printing resolution, 2 kHz jetting frequency) and then put on a thermocouple-controlled hotplate in air at 180 °C for 1 h. The np-SnO$_x$ (Alfa Aesar, stable dispersion in water, diluted with DI water to 2.5 wt%) references were prepared via spin-coating (4000 rpm, 30s in air) and annealed at 250 °C for 30 min. The TCP absorber layers were deposited by inkjet printing (1100 dpi, 2–5 kHz) and then within ≈30 s transferred to a nearby vacuum chamber (Pfeiffer Vacuum Technology AG) which was evacuated down to 5 × 10^{-2} mbar. When the perovskite was formed the chamber was slowly vented and the samples were placed on a hotplate at 100 °C for annealing. Spiro-OMeTAD was deposited as HTL by spin coating (4000 rpm, 30 s) and left for oxygen doping overnight in a dry box. Devices were finalized by evaporating a ≈75 nm gold rear-electrode through a shadow-mask, defining the active area to 10.5 mm².

Perovskite Solar Cells Characterization: The solar cell characteristics were measured with an AM1.5G spectrum at 100 mW cm^{-2} using a class AAA xenon-lamp-based solar simulator (Newport Oriel Sol3A) or a class AAA 21-channel LED solar simulator (Wavelabs Solar Metrology Systems GmbH), both inside a nitrogen-filled glovebox. For calibration, a KG5 short pass-filtered silicon reference solar cell was used. The JV-scans of the cells were measured in both backward and forward direction with a constant scan rate of ≈0.6 V s^{-1} (Keithley 2400 source measurement unit). The temperature of the solar cell was controlled (25 °C) using a microcontroller-adjusted Peltier-element.

Supporting Information

Supporting Information is available from the Wiley Online Library or from the author.

Acknowledgements

Conflict of Interest

The authors declare no conflict of interest.

Keywords

[1] A. Kojima, K. Teshima, Y. Shirai, T. Miyasaka, *J. Am. Chem. Soc.* **2009**, *131*, 6050.

[2] Z. Song, S. C. Watthage, A. B. Phillips, M. J. Heben, *J. Photonics Energy* **2016**, *6*, 022001.

[3] Best Research-Cell Efficiency Chart | Photovoltaic Research | NREL, https://www.nrel.gov/pv/cell-efficiency.html (accessed: April 2020).

[4] L. Xiong, Y. Guo, J. Wen, H. Liu, G. Yang, P. Qin, G. Fang, *Adv. Funct. Mater.* **2018**, *28*, 1802757.

[5] M. Batzill, U. Diebold, *Prog. Surf. Sci.* **2005**, *79*, 47.

[6] V.-H. Tran, R. B. Ambade, S. B. Ambade, S.-H. Lee, I.-H. Lee, *ACS Appl. Mater. Interfaces* **2017**, *9*, 1645.

[7] M. F. Aygüler, A. G. Hufnagel, P. Rieder, M. Wussler, W. Jaegermann, T. Bein, V. Dyakonov, M. L. Petrus, A. Baumann, P. Docampo, *ACS Appl. Mater. Interfaces* **2018**, *10*, 11414.

[8] D. Liu, Y. Wang, H. Xu, H. Zheng, T. Zhang, P. Zhang, F. Wang, J. Wu, Z. Wang, Z. Chen, S. Li, *Sol. RRL* **2019**, *3*, 1800292.

[9] S. Trost, A. Behrendt, T. Becker, A. Polywka, P. Görrn, T. Riedl, *Adv. Energy Mater.* **2015**, *5*, 1500277.

[10] J. Duan, Q. Xiong, B. Feng, Y. Xu, J. Zhang, H. Wang, *Appl. Surf. Sci.* **2017**, *391*, 677.

[11] D. Kohl, *Sens. Actuators* **1989**, *18*, 71.

[12] I. Paulowicz, V. Hrkac, S. Kaps, V. Cretu, O. Lupan, T. Braniste, V. Duppel, I. Tiginyanu, L. Kienle, R. Adelung, Y. K. Mishra, *Adv. Electron. Mater.* **2015**, *1*, 1500081.

[13] W. Ke, G. Fang, Q. Liu, L. Xiong, P. Qin, H. Tao, J. Wang, H. Lei, B. Li, J. Wan, G. Yang, Y. Yan, *J. Am. Chem. Soc.* **2015**, *137*, 6730.

[14] L. Xiong, Y. Guo, J. Wen, H. Liu, G. Yang, P. Qin, G. Fang, *Adv. Funct. Mater.* **2018**, *28*, 1802757.

[15] L. Yang, A. T. Barrows, D. G. Lidzey, T. Wang, *Rep. Prog. Phys.* **2016**, *79*, 026501.

[16] F. Mathies, E. J. W. List-Kratochvil, E. L. Unger, *Energy Technol.* **2020**, *8*, 1900991.

[17] J. P. Correa-Baena, M. Saliba, T. Buonassisi, M. Grätzel, A. Abate, W. Tress, A. Hagfeldt, *Science* **2017**, *358*, 739.

[18] W. Ke, D. Zhao, A. J. Cimaroli, C. R. Grice, P. Qin, Q. Liu, L. Xiong, Y. Yan, G. Fang, *J. Mater. Chem. A* **2015**, *3*, 24163.

[19] M. Ohyama, H. Kozuka, T. Yoko, S. Sakka, *J. Ceram. Soc. Jpn.* **1996**, *104*, 296.

[20] H. A. Ávila, J. E. Rodríguez-Páez, *J. Non-Cryst. Solids* **2009**, *355*, 885.

[21] R. Al-Gaashani, S. Radiman, N. Tabet, A. R. Daud, *Mater. Sci. Eng., B* **2012**, *177*, 462.

[22] P. S. Patil, R. K. Kawar, T. Seth, D. P. Amalnerkar, P. S. Chigare, *Ceram. Int.* **2003**, *29*, 725.

[23] H. Deng, F. J. Lamelas, J. M. Hossenlopp, *Chem. Mater.* **2003**, *15*, 2429.

[24] D. W. Berreman, *Phys. Rev.* **1963**, *130*, 2193.

[25] B. H. Stuart, *Infrared Spectroscopy: Fundamentals and Applications*, Wiley Online Library, Wiley, New York, USA **2005**.

[26] B. X. Huang, P. Tornatore, Y.-S. Li, *Electrochim. Acta* **2001**, *46*, 671.

[27] J. Geurts, S. Rau, W. Richter, F. J. Schmitte, *Thin Solid Films* **1984**, *121*, 217.

[28] P. Loose, M. Wöhlecke, M. Rölker, M. Rosenzweig, *Solid State Commun.* **1976**, *19*, 231.

[29] R. Summitt, *J. Appl. Phys.* **1968**, *39*, 3762.

[30] F. Bréhat, B. Wyncke, J. M. Léonard, Y. Dusausoy, *Phys. Chem. Miner.* **1990**, *17*, 191.

[31] R. S. Katiyar, P. Dawson, M. M. Hargreave, G. R. Wilkinson, *J. Phys. C: Solid State Phys.* **1971**, *4*, 2421.

[32] K. T. Queeney, M. K. Weldon, J. P. Chang, Y. J. Chabal, A. B. Gurevich, J. Sapjeta, R. L. Opila, *J. Appl. Phys.* **2000**, *87*, 1322.

[33] F. Ullrich, S. Hillebrandt, S. Hietzschold, V. Rohnacher, T. Marszalek, W. Kowalsky, R. Lovrincic, S. Beck, E. Mankel, A. Pucci, *ACS Appl. Energy Mater.* **2018**, *1*, 3113.

[34] E. W. Thornton, P. G. Harrison, *J. Chem. Soc., Faraday Trans. 1* **1975**, *71*, 461.

[35] F. Ullrich, *Dissertation*, TU Darmstadt, Germany, January **2020**.

[36] Q. Jiang, L. Zhang, H. Wang, X. Yang, J. Meng, H. Liu, Z. Yin, J. Wu, X. Zhang, J. You, *Nat. Energy* **2017**, *2*, 16177.

[37] E. H. Anaraki, A. Kermanpur, L. Steier, K. Domanski, T. Matsui, W. Tress, M. Saliba, A. Abate, M. Grätzel, A. Hagfeldt, J. P. Correa-Baena, *Energy Environ. Sci.* **2016**, *9*, 3128.

[38] M. Saliba, J. P. Correa-Baena, C. M. Wolff, M. Stolterfoht, N. Phung, S. Albrecht, D. Neher, A. Abate, *Chem. Mater.* **2018**, *30*, 4193.

[39] I. A. Howard, T. Abzieher, I. M. Hossain, H. Eggers, F. Schackmar, S. Ternes, B. S. Richards, U. Lemmer, U. W. Paetzold, *Adv. Mater.* **2019**, *31*, 1806702.

[40] LG Display to start pilot production of ink-jet OLEDs in 2017 | OLED-Info, https://www.oled-info.com/lg-display-start-pilot-production-ink-jet-oleds-2017 (accessed: March 2020).

[41] Inkjet OLED Technology on the Verge of Mass Production, with Capacity Set to Rise 12-Fold from 2020 to 2024 - Omdia, https://technology.informa.com/615284/inkjet-oled-technology-on-the-verge-of-mass-production-with-capacity-set-to-rise-12-fold-from-2020-to-2024 (accessed: March 2020).

[42] Kateeva Introduces OLED RBG Pixel Deposition Line-up – LEDinside, https://www.ledinside.com/products/2017/11/kateeva_introduces_oled_rbg_pixel_deposition_line_up (accessed: March 2020).

[43] H. C. Nallan, J. A. Sadie, R. Kitsomboonloha, S. K. Volkman, V. Subramanian, *Langmuir* **2014**, *30*, 13470.

[44] S. Gharibzadeh, B. Abdollahi Nejand, M. Jakoby, T. Abzieher, D. Hauschild, S. Moghadamzadeh, J. A. Schwenzer, P. Brenner, R. Schmager, A. A. Haghighirad, L. Weinhardt, U. Lemmer, B. S. Richards, I. A. Howard, U. W. Paetzold, *Adv. Energy Mater.* **2019**, *9*, 1803699.

[45] Y. N. Kim, H. G. Shin, J. K. Song, D. H. Cho, H. S. Lee, Y. G. Jung, *J. Mater. Res.* **2005**, *20*, 1574.

[46] A. J. Huckaba, Y. Lee, R. Xia, S. Paek, V. C. Bassetto, E. Oveisi, A. Lesch, S. Kinge, P. J. Dyson, H. Girault, M. K. Nazeeruddin, *Energy Technol.* **2019**, *7*, 317.

[47] A. Gheno, Y. Huang, J. Bouclé, B. Ratier, A. Rolland, J. Even, S. Vedraine, *Sol. RRL* **2018**, *2*, 1800191.

[48] C. Liang, P. Li, H. Gu, Y. Zhang, F. Li, Y. Song, G. Shao, N. Mathews, G. Xing, *Sol. RRL* **2018**, *2*, 1770150.

[49] W. Theiss, SCOUT - Software Package for Optical Spectroscopy. WTheiss Hardware and Software, 11875 E Elin Ranch Road, Tucson, AZ 85749, USA, http://www.wtheiss.com (accessed: April 2018).

[50] H. Eggers, F. Schackmar, T. Abzieher, Q. Sun, U. Lemmer, Y. Vaynzof, B. S. Richards, G. Hernandez-Sosa, U. W. Paetzold, *Adv. Energy Mater.* **2020**, *10*, 1903184.